AIMS Geosciences

AIMS Geosciences, 3 (3): 352-374
DOI: 10.3934/geosci.2017.3.352
Received date 12 May 2017
Accepted date 04 August 2017
Published date 10 August 2017

http://www.aimspress.com/journal/geosciences

Research article

Investigating the Surface and Subsurface in Karstic Regions – Terrestrial Laser Scanning versus Low-Altitude Airborne Imaging and the Combination with Geophysical Prospecting

Nora Tilly * and Daniel Kelterbaum

Institute of Geography, University of Cologne, Germany

* **Correspondence:** Email: nora.tilly@uni-koeln.de; Tel: +49-0221-470-89653.

Abstract: Combining measurements of the surface and subsurface is a promising approach to understand the origin and current changes of karstic forms since subterraneous processes are often the initial driving force. A karst depression in south-west Germany was investigated in a comprehensive campaign with remote sensing and geophysical prospecting. This contribution has two objectives: firstly, comparing terrestrial laser scanning (TLS) and low-altitude airborne imaging from an unmanned aerial vehicle (UAV) regarding their performance in capturing the surface. Secondly, establishing a suitable way of combining this 3D surface data with data from the subsurface, derived by geophysical prospecting. Both remote sensing approaches performed satisfying and the established digital elevation models (DEMs) differ only slightly. These minor discrepancies result essentially from the different viewing geometries and post-processing concepts, for example whether the vegetation was removed or not. Validation analyses against high-accurate DGPS-derived point data sets revealed slightly better results for the DEM_{TLS} with a mean absolute difference of 0.03 m to 0.05 m and a standard deviation of 0.03 m to 0.07 m (DEM_{UAV}: mean absolute difference: 0.11 m to 0.13 m; standard deviation: 0.09 m to 0.11 m). The 3D surface data and 2D image of the vertical cross section through the subsurface along a geophysical profile were combined in block diagrams. The data sets fit very well and give a first impression of the

connection between surface and subsurface structures. Since capturing the subsurface with this method is limited to 2D and the data acquisition is quite time consuming, further investigations are necessary for reliable statements about subterraneous structures, how these may induce surface changes, and the origin of this karst depression. Moreover, geophysical prospecting can only produce a suspected image of the subsurface since the apparent resistivity is measured. Thus, further measurements, such as borehole drillings or ground-penetrating radar are necessary for a closer analysis of the subsurface. In summary, satisfying results were achieved, which however pave the way for further studies.

Keywords: Terrestrial laser scanning; low-altitude airborne imaging; digital elevation model; high-resolution mapping; geoelectric; electrical resistivity tomography; karst landscape

1. Introduction

Major applications of remote sensing in geoscience are detecting and monitoring geomorphological structures. Generally, the overall aim of most geomorphological studies is assessing terrain features in an area of interest (AOI) with a sufficiently high topographic and objective differentiation [1]. Innovations and technical progresses in the field of remote sensing caused a rapid increase in the number of available sensors and methods of capturing surfaces in 3D. Even though these remote sensing methods allow a reliable surface mapping, investigating the subsurface is almost impossible. This would however be beneficial for investigations in which surface changes might be explainable by subterraneous processes. Hence, it is desirable to combine surface and subsurface data.

Investigations in karstic regions are one example where such combined investigations should be worthwhile, since subterraneous solution and subsidence processes are likely to cause surfaces changes. In this study, a karst depression in south-west Germany was investigated, where surface changes are expected based on human-based long-term observations. Monitoring campaigns with terrestrial laser scanning (TLS) during the last two years, have however not shown discernible movements yet [2]. This detection of temporal changes is not the primary topic of this contribution. Instead, the focus lies on a better understanding of the surface and subsurface structures and their interrelation. Strictly speaking, the results of a comprehensive campaign are presented, where TLS and low-altitude airborne imaging from an unmanned aerial vehicle (UAV) were applied for capturing the surface, and electrical resistivity tomography (ERT) was conducted for imaging subsurface structures. This contribution follows two aims: (I) investigating the usability of both remote sensing systems for capturing fine karstic structures and (II) establishing a suitable way of combining the surface mapping with the data from the subsurface and examining its benefit. The latter presupposes the visualization of the ERT measurements.

1.1. Capturing the surface

A large number of remote sensing approaches already exist for capturing surfaces in 3D. With regard to the topic of this paper, a short introduction into laserscanning and into low-altitude airborne imaging are in the focus of this paragraph. Measurements based on Light Detection and Ranging (LiDAR) are generally widely applied due to their known accuracy and reliability [3]. LiDAR measurements may be performed as airborne laser scanning (ALS) or terrestrial laser scanning (TLS) depending on factors such as the targeted spatial and temporal resolution, the desired level of detailedness, or the extent and accessibility of the AOI. Examples for both methods can be widely found [4–6]. Even though TLS measurements are considerably cheaper and easier to perform than ALS approaches, the effort and expense should still not be underestimated. Beside the costs, major issues are the unsuitability in terrains with difficult access or the time requirement.

An important step in the evolution of remote sensing was the development of UAVs as platform for different remote sensing sensors over the last several years. Further benefited by the rapidly increasing quality of affordable conventional digital cameras, a growing research interest on low-cost UAV-based imaging for scientific studies can be determined [7,8]. Key features of most approaches are to be as flexible and time- and cost-effective as possible. Moreover, areas which are not or less accessible with ground-based sensors can be investigated. The captured images are commonly used to derive 3D information based on the structure from motion (SfM) approach [9,10]. Only little research has however been done so far on the accuracy and reliability of collected data in comparison to traditional remote sensing methods. The integration of UAV-based photogrammetry and TLS for the mapping of open-pit mine areas for example was performed by Tong et al. [11]. Moreover, Smith et al. [12] and Ouédraogo et al. [13] outlined the benefits and challenges of low-altitude airborne imaging for studies in physical geography. Nevertheless, the widespread and further growing number of available systems still requires research focusing on the practical application. Moreover, validation analyses against reliable reference data are required. Comparative studies with trustworthy data and measuring procedures are therefore necessary.

1.2. Investigating the subsurface

Capturing information about the subsurface is generally more difficult than investigations of the surface since the access is obviously limited. Different approaches of deriving information exist, which can be divided into destructive and non-destructive methods. The latter ones are often based on near-surface geophysical prospection methods, such as ground penetrating radar, seismic surveying, or electrical resistivity tomography (ERT) [14]. A major advantage of these non-destructive measurements is that, information can be gained without disturbing the subsurface. Moreover, with most of the methods quite large areas can be assessed in a short time. In this study, ERT measurements were performed, as they are known for their suitability in karstic regions [15–17].

Moreover, ERT was already successfully used in combination with TLS [18,19]. The result of an ERT profile is a visualization of the suspected subsurface, derived from the measured apparent resistivity. This 2D image can indicate the existence of different layers in the subsurface. The resistivity values are plotted as pseudosections, resulting from an inversion model. Thus, these pseudosections can show the variation of the measured resistivity in relation to the position and the effective depth of penetration but cannot show the exact depths of layer borders. Moreover, the material of the subsurface cannot be determined from ERT measurements alone.

In contrast, destructive measurements, such as borehole drillings, can be used for specific statements about the material of the subsurface or the depths of layer borders. Borehole drilling is a commonly used method of investigating the subsurface and also applied in karstic regions [17,20]. A major limitation of borehole drilling is that only data at single locations can be achieved in a time consuming process, which limits the recordable data in a short campaign. Overall, an efficient approach should base on the combination of geophysical prospecting and borehole drilling.

2. Materials and Methods

2.1. Study area

Large parts of the land surface which are today located in the temperate zone of central Europe were situated in the subtropics and below sea level during the Triassic, lasting from ~230 to ~195 million years BP [21]. Calcareous sediments, shells, and other marine features were hence deposited under marine environs and later fossilized. This is also indicated by the name of this lithostratigraphic unit *Muschelkalk* (shellbearing limestone), which covers the older *Buntsandstein* (colorful sandstone) and lies below the younger *Keuper*. Outcrops of *Muschelkalk* can be found in Middle and South Germany, where weathering of the limestone induces the development of karstic phenomena. Such regions are marked by sinkholes, ponors, or karst depressions [1].

In this study, an episodically water-filled karst depression, named *Ottensee*, in the region of Hohenlohe in the German federal state Baden-Württemberg was investigated (Figure 1). The area, which is protected as a small nature reserve, is about 100 m by 200 m in size and embedded in a larger and geologically older valley [22]. The area surrounded by the trees (Figure 1 top) can roughly be regarded as AOI. Since only a very small part of the depression is constantly filled with water, the rest of the area is used for pasture farming. However, torrential rain and the consequential subterranean run-off through southern lying higher aquifers cause a flooding of the depression from time to time. This results in a small lake, which lasts for a few hours to weeks, depending on the filling level and the general natural inflow. Then the water drains off through ponors in the northern part of the depression, where the entire terrain is also a bit lower. This episodic flooding is likely to change the surface and to induce dissolution processes in the subsurface.

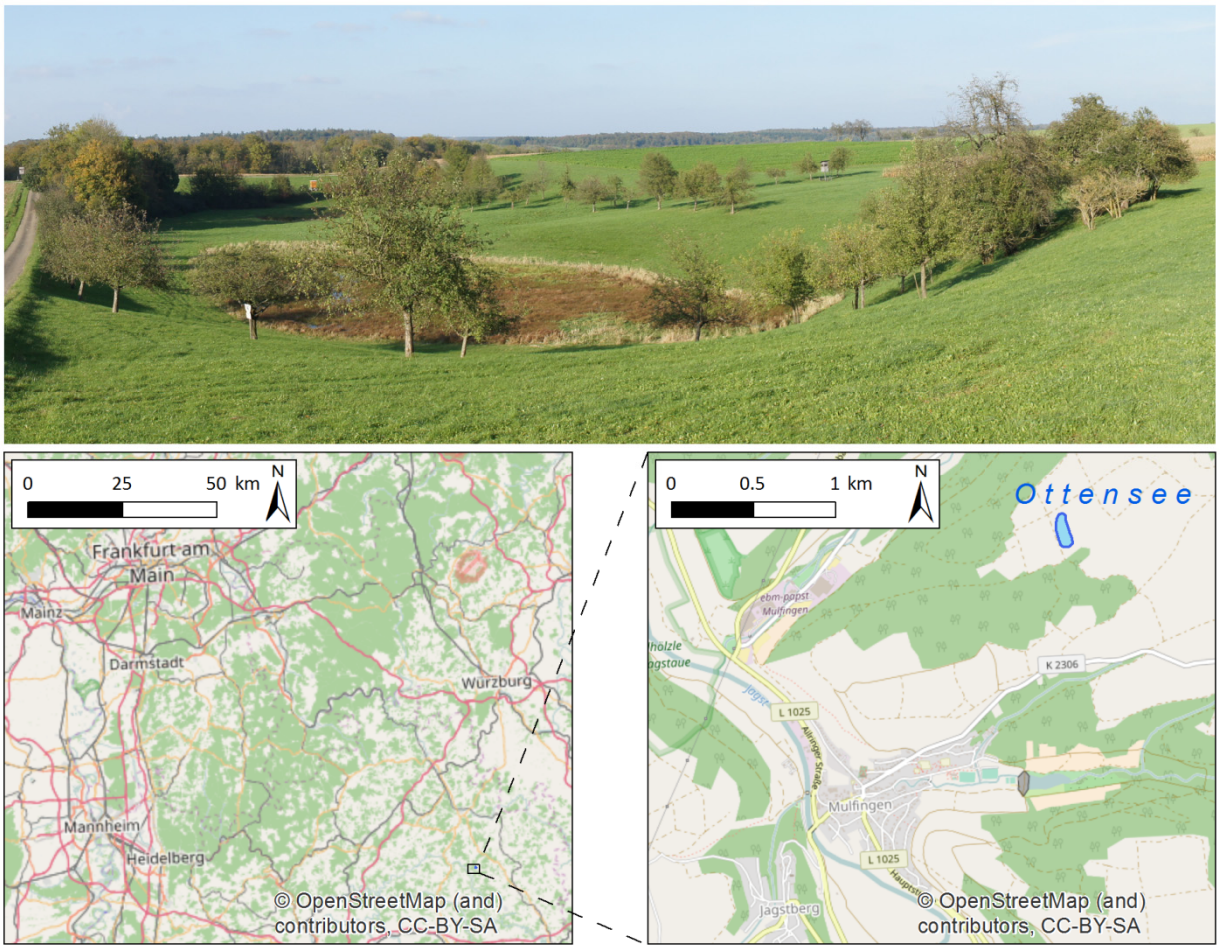

Figure 1. Karst depression *Ottensee* in the region of Hohenlohe, Baden-Württemberg. Top: Picture captured from the south side. Area surrounded by the trees can roughly be regarded as AOI. Bottom: Map of the closer region (right) and its location in the South of Germany (left).

2.2. Data acquisition

An extensive field campaign was carried out between the 26th and 29th of May 2016. The surface was almost continuously captured in 3D with terrestrial laser scanning and low-altitude airborne imaging. The pasture in the AOI was previously mown for an easier detection of the bare ground. Several point measurements were carried out with the high-accurate differential global positioning system (DGPS) device Topcon HiPer Pro [23] for acquiring two reference point data sets. A relative accuracy of 1 cm is reached with this device. The subsurface was investigated with geoelectrical measurements. As mentioned above, such ERT profiles can only provide a suspected 2D image of the subsurface derived from the measured apparent resistivity and illustrate the existence of different layers or structures in the subsurface. Hence, borehole drilling was performed to analyze the material of the subsurface and detecting the specific depths of layer borders. These analyses were however neglected in this contribution, due to the focus on imaging methods. The

general detection of subsurface structures from the ERT measurements and their interrelation with the surface data were of primary importance.

2.2.1. Capturing the surface

Laser scanning was performed using the Riegl LMS-Z420i with the digital camera Nikon D200 mounted on top [24]. This time-of-flight scanner applies a near-infrared laser beam with a beam divergence of 0.25 mrad. It can record up to 11,000 points/sec with a field of view up to 80 ° in the vertical and 360 ° in the horizontal direction. In this study, a resolution of 0.04 ° was used. The point clouds gained from the laser scanner can be colorized from the images taken by the camera. Six scan positions were established to attain an almost uniform spatial coverage of the whole AOI (marked in Figure 2). The coordinates of the scan positions and additional reference targets were measured with the DGPS device. These targets are required for the georeferencing and merging of the positions in the post-processing. Highly reflective cylinders arranged on ranging poles act as reference targets. They can be easily detected by the scanner and thus their exact position in relation to the scan position can be measured.

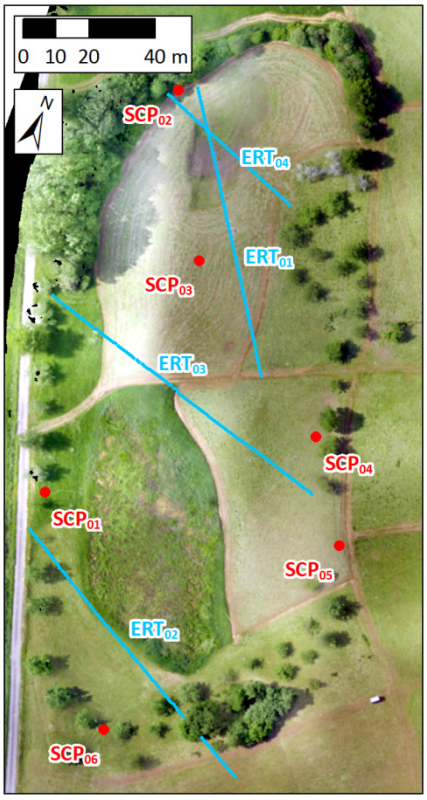

Figure 2. Orthophoto of the *Ottensee* derived from the UAV-based imaging. Scan positions (SCP) marked in red and electrical resistivity tomography (ERT) profiles marked in blue.

In contrast to the expensive TLS system, a low-cost approach was pursued for the low-altitude airborne imaging. The DJI Phantom 3 Professional was therefore used [25]. This UAV is equipped with a camera, which is attached via a gimbal and thus stabilized in the three axes (roll, pitch, and yaw). The camera has a 1/2.3" CMOS sensor with an effective number of pixels of 12.4 M and a 94 ° field of view. During the campaign, the UAV was remotely piloted with the included controller and the DJI GO app [26], installed on an attached tablet PC. The real-time downlink during the flight allows seeing exactly which area is covered. Moreover, software options enable to define waypoints. During the final image acquisition, the thereby predefined flight paths can be controlled by an autopilot. Hence, a constant height and speed can be ensured. Since the maximal flight time of the Phantom 3 with one battery pack is about 23 minutes, two battery packs were necessary for the entire acquisition process. The final image capturing was carried out in 38 m altitude with a speed of 0.8 m/s and continuous shooting (1 image per 5 sec). About 200 images were taken to cover the AOI. This resulted in an image overlap of > 9 in almost the entire area and a ground resolution of 1.32 cm/pixel. Before the flight, 50 ground control points (GCPs) were distributed in the AOI and their coordinates were measured with the DGPS device. These GCPs can be detected in the images during the post-processing and are used to enhance the georeferencing.

2.2.2. Investigating the subsurface

Electrical resistivity tomography (ERT) was carried out with the multi-electrode system GeoTomMK8E1000RES/IP/SP [27]. Four ERT profiles were taken with lengths of 50 m to 100 m and electrode spacings of 0.5 m to 1.0 m (marked in Figure 2). The exact position of each electrode was measured with the DGPS device for a topographic correction of the data in the post-processing. Various measuring methods and arrangements are generally possible, differing in features, such as electrode spacing and design [28,29]. The Wenner array is known of having a high sensitivity to vertical resistivity changes and is well suitable for detecting horizontal structures [30,31]. Thus, it was used in this study. The result of one ERT measurement is a 2D image of the vertical cross section, showing the apparent resistivity. They are referred to as 2D images of apparent resistivity in the following.

2.3. Data analysis

During the field campaign an extensive data set was acquired, including: (I) one TLS point cloud per scan position, (II) the coordinates of these scan positions, (III) all single images from the low-altitude airborne imaging, (IV) the coordinates of the GCPs, (V) two reference point data sets, (VI) four 2D images of apparent resistivity from the ERT profiles, and (VII) the coordinates of each electrode. Consequently, the post-processing and analysis process were quite extensive, involving overall eight software programs as shown in the workflow (Figure 3). According to the

aims stated at the beginning, this complex scheme could be divided into two main analysis paths, which will be explained in the following. The first aim was mapping the surface from the TLS data and from the UAV-derived images, compare the results, and validate them with the reference data sets. The second aim was combining the surface visualization with the suspected image of the subsurface. Prior to that, visualizing the subsurface was necessary.

2.3.1. Surface visualization

The scanner software RiSCAN Pro was applied for the first post-processing steps of the TLS data (Figure 3 center top). A software implemented terrain filter was used to remove most of the vegetation, complemented by a manual editing. Then the AOI was extracted. A common way for analyzing and presenting such data is the visualization as digital elevation models (DEMs). Hence, after importing the point cloud to Esri ArcMap 10.4.1, a raster data set containing the height values was created using the inverse distance weighting (IDW) algorithm. IDW is an exact, deterministic algorithm. The accuracy of measurements with a high density is maintained, since it retains measured values at their discrete sample location [32]. The result of the interpolation is a DEM raster data set.

All single UAV-derived images were merged to an orthophoto and the DEM covering the entire area was generated with the SfM-based software Agisoft PhotoScan 1.2.0 (Figure 3 right top). A coarse georeferencing is already achievable with the GPS information stored for each image. The DGPS-derived coordinates of the GCPs were however used to enhance this georeferencing. The final DEM was exported and then ArcMap was used to extract the AOI in conformity with the DEM_{TLS}.

Due to the different acquisition methods, the resulting point densities and distributions were quite heterogeneous in the AOI. The TLS-and UAV-derived raster data sets were resampled to a common resolution of 0.05 m, which can still be regarded as being a sufficiently high resolution for this study. The difference between these comparable DEMs was calculated with the ArcGIS raster calculator. The result is a raster data set, showing the spatially resolved difference between the DEM_{TLS} and the DEM_{UAV}. This raster data set as well as the DEM_{TLS} and DEM_{UAV} were finally cartographically illustrated and exported.

The DGPS-derived reference data sets were used for validating the DEMs. Two data sets, namely set A and B, were acquired with 20 and 18 points, respectively (Figure 3 very right). It has to be mentioned that set A was already part of the GCPs for the georeferencing of the UAV-derived orthophoto. Hence, this data set is only for the DEM_{TLS} a completely independent reference. Both data sets were converted to vector point data for automatically extracting the height values from the DEMs. The minimum height of the respective DEM was extracted for a created buffer area around each point (radius of 0.20 m). These values were used to prevent overestimations caused by remaining vegetation in the calculated DEMs. In addition, the standard deviation per buffer area

was calculated to check whether the extracted heights could be regarded as representative for their particular location. Finally, these DEM heights were validated against the DGPS-derived heights of the reference data sets.

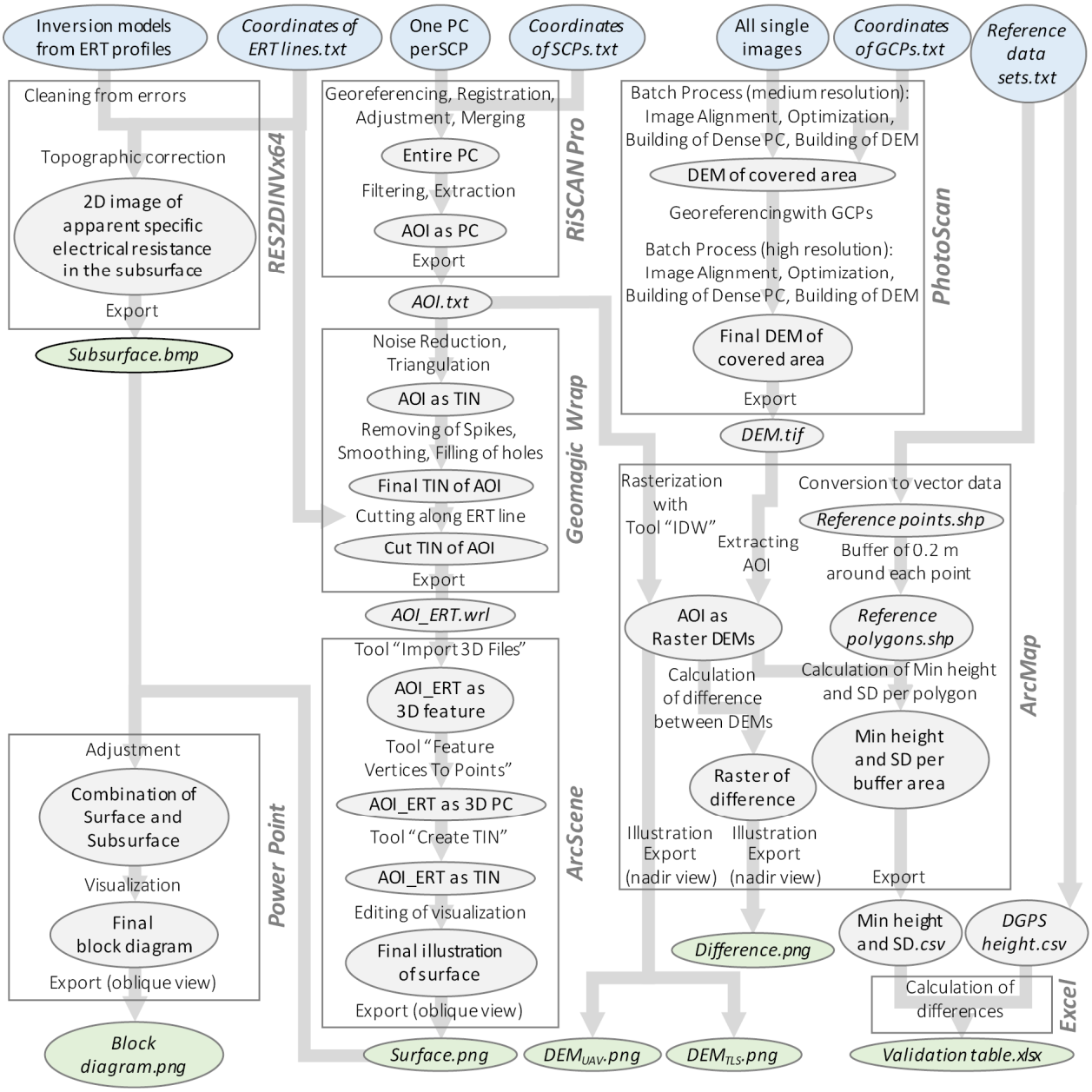

Figure 3. Workflow of the the post-processing and analysis process. The following abbreviations are used: Area of interest (AOI); Differential global positioning system (DGPS); Digital elevation model (DEM); Electrical resistivity tomography (ERT); Ground control points (GCPs); Inverse distance weighting (IDW); Minimum (Min); Point cloud (PC); Scan position (SCP); Standard deviation (SD); Terrestrial laser scanning (TLS); Triangulated irregular network (TIN); unmanned aerial vehicle (UAV).

2.3.2. Subsurface visualization

The 2D images of apparent resistivity achieved from the ERT profiles were post-processed with the RES2DINVx64 software [33] (Figure 3 left top). This post-processing included a cleaning of errors (values with a standard deviation > 5 %) and the topographic correction of the surface contour. The latter was based on the DGPS-derived coordinates of each electrode. Such topographic corrections are recommended in the case of considerable altitudinal differences or complex relief structures for a better positioning of the measured values in the subsurface. Moreover, the correct surface contour is necessary for merging the images of the subsurface with the surface data. The measured apparent resistance values were inverted according to the method of Loke & Barker [34] for a rapid least-square model optimized by a quasi-Newton method. An initial model of the subsurface, consisting of the same number of rectangular blocks as measuring points, is optimized in several iterations to minimize the difference between measured and calculated values.

2.3.3. Combination of surface and subsurface data

The created raster DEMs are sufficient for exclusively visualizing the surface and a resultant interpretation and validation. They are however less suitable for visualizations with an oblique viewing perspective on the surface, which is necessary for the combination with the 2D images of the subsurface in a block diagram. Triangulated irregular networks (TINs) are recommendable for such pseudo 3D visualizations. For this first approach, the TLS-derived point cloud was used, as it better presents the bare ground of the karst depression since the vegetation was removed. The UAV-derived data set was neglected so far, but in principle, a similar approach can be carried out.

A first attempt was made to create a TIN_{TLS} with the software tools in Esri ArcScene 10.4.1. Unfortunately, the result was very edgy with sharp corners and could not be regarded as realistic depiction of the surface. Thus, an additional software, namely Geomagic Wrap 2015.1.3, was applied (Figure 3 center). This software can be used to transform 3D scan data into 3D models with a stronger focus on computer-aided design (CAD) features than in ArcScene. After importing the TLS point cloud, a noise reduction was executed and the resulting point cloud was triangulated to a TIN_{TLS}. Software implemented functions were then used for removing spikes, smoothing the surface, and filling holes in the mesh. The coordinates of two ERT profiles were also imported. The final TIN_{TLS} was cut along these lines for the later visualization in block diagrams.

From this processing, a realistic depiction of the supposed bare surface could be achieved, but for the final visualization further features were desired, such as a coloring of the TIN_{TLS} by height and a vertical exaggeration of the TIN_{TLS}. A transfer of the data to ArcScene was necessary, since this was not possible in Geomagic Wrap. As shown in the bottom center of Figure 3, a series of tools from the ArcGIS toolbar was therefore necessary. Finally, the cartographically illustrated TIN_{TLS} with a vertical exaggeration of 1.5 was exported as image with an oblique viewing perspective on the

surface. Generally, any image processing software can then be used to combine this pseudo 3D visualization and the 2D image of the apparent resistivity in the subsurface. In this study, Microsoft PowerPoint 2016 was used (Figure 3 left bottom). The images of the surface and subsurface were adjusted and finally visualized as block diagram.

3. Results and Discussion

Terrestrial laser scanning and low-altitude airborne imaging were performed for capturing the surface of the karst depression *Ottensee* in a high resolution. Due to the almost simultaneous acquisition, comparing both models is possible and the DGPS-derived reference data sets allowed validating the measured heights. In addition, geoelectrical measurements were performed for investigating the subsurface. Finally, the combined visualization of these data sets aims to increase the understanding of the connection between surface and subsurface structures. According to the workflow, in the following the derived DEMs are presented and discussed first, followed by discussing the images of the subsurface. Finally, the combined visualization as block diagram is assessed.

3.1. Digital elevation models

A common way to present the surface of a terrain captured by remote sensing is to visualize the achieved DEM as raster data set colored by height. Such maps were generated for the DEM_{TLS} (Figure 4A) and the DEM_{UAV} (Figure 4B). Figure 4C) shows the spatially calculated difference between the DEMs to compare the results of both sensors. In general, the differences between the DEMs are quite marginal. Since the vegetation was however not removed in the low-altitude airborne imaging approach, the height values are mostly slightly higher than in the TLS-derived model. In particular, the trees at the edges of the AOI cause very high values. Differences between the DEMs larger than 1 m were excluded from the classification since they can be regarded as error due to the vegetation (grey color in Figure 4C). In most parts of the AOI the difference between the DEMs is less than 25 cm (very light red/ green in Figure 4C), or even less than 10 cm (off-white in Figure 4C).

As already mentioned for Figure 1 the AOI can be roughly defined by the trees at the edges of the depression. This area can be described as kidney-shaped valley with a flat hollow in the southern part and a deeper one in the norther part. The southern one is almost constantly filled with water, allowing sedge and reeds to grow there. This vegetation is mainly responsible for the differences between the DEMs. The nadir perspective of the UAV-based camera allows capturing very low points between the vegetation, which cannot be reached from the oblique perspective of the laser scanner. However, since the vegetation was removed from the TLS-derived point cloud the DEM_{TLS} shows a smooth surface in this area. In contrast, the DEM_{UAV} shows a rougher surface

with high values due to the remaining vegetation and low values from the ground between it. The northern hollow is generally deeper and only covered by pasture, as the rest of the AOI. Hence, the DEMs are more similar with quite small differences in this part.

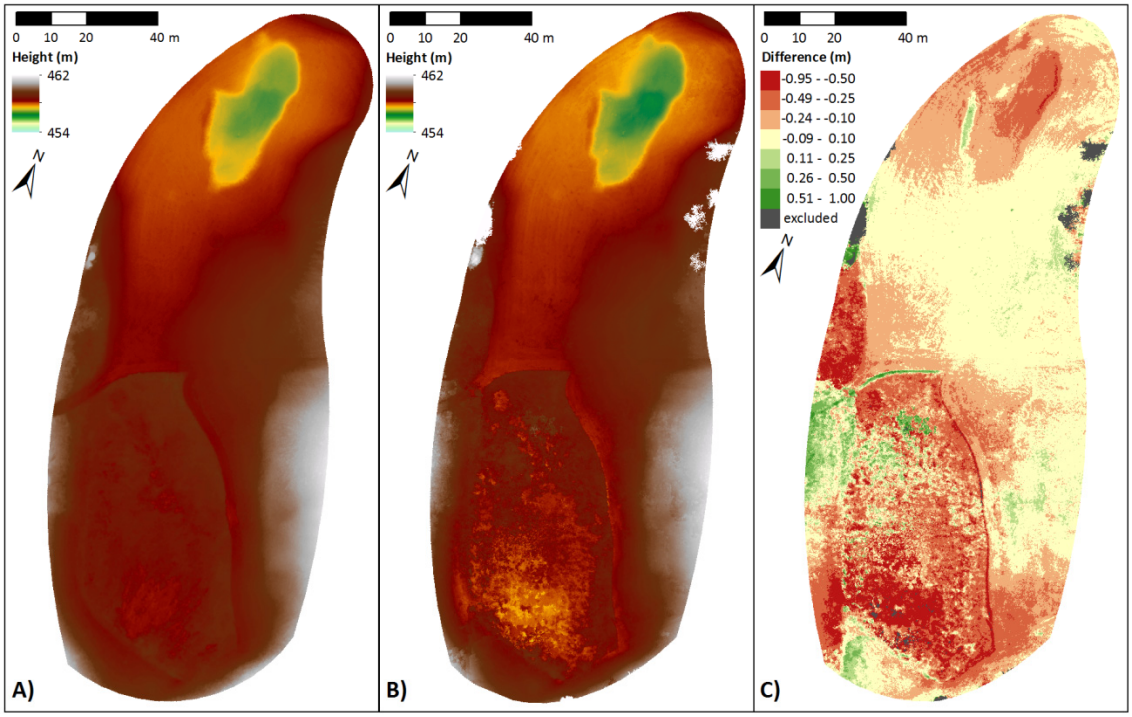

Figure 4. Digital elevation models (DEMs) as raster data sets, derived by A) Terrestrial laser scanning and B) low-altitude airborne imaging. Height values > 462 m were excluded from the color ramp and colored in white as they are caused by trees. C) Spatially calculated difference between both raster data sets, calculated by subtracting the DEM_{TLS} from the DEM_{UAV}.

The DGPS-derived reference data sets were used for validating the DEMs (Table 1). While both data sets are an independent reference for validating the DEM_{TLS}, set A was already used for the georeferencing of the DEM_{UAV} and had thus an influence on the accuracy of this model already. The minimum height and standard deviation in the circular buffer area around each reference point are given for both DEMs. The standard deviation (SD) is with 0.01 m to 0.04 m per buffer area very low and thus, the stated values can be regarded as representative for the particular location. In addition to the difference between the DEM height and the vertical coordinate of each reference point (Z), the absolute value is given for a more reliable comparability of the discrepancies. The DEM_{TLS} can generally be regarded as being accurate with a mean absolute difference of 0.05 m and 0.03 m and SD values of 0.07 m and 0.03 m for set A and B, respectively. The discrepancies between the DEM_{UAV} and the reference data sets are generally slightly higher with a mean absolute difference of 0.13 m and 0.11 m and SD values of 0.11 m and 0.09 m for set A and B, respectively.

Table 1. Validation of the digital elevation models (DEMs) against the reference data sets. Set A was already used for the georeferencing of the DEM_{UAV} and can thus only be regarded as independent validation for the DEM_{TLS} (*Z*: vertical coordinate of reference point; SD: standard deviation; Diff.: Difference; Abs. Diff.: Absolute difference).

Reference data sets		*DEM_{TLS}*				*DEM_{UAV}*			
Name	*Z (m)*	*Height (m)*	*SD (m)*	*Diff. (m)*	*Abs. Diff. (m)*	*Height (m)*	*SD (m)*	*Diff. (m)*	*Abs. Diff. (m)*
Set-A_P01	459.97	459.93	0.02	0.04	0.04	459.87	0.03	0.10	0.10
Set-A_P02	460.43	460.28	0.04	0.16	0.16	460.18	0.03	0.26	0.26
Set-A_P03	460.89	460.88	0.02	0.01	0.01	460.94	0.02	-0.05	0.05
Set-A_P04	458.55	458.60	0.02	-0.05	0.05	458.52	0.01	0.02	0.02
Set-A_P05	458.62	458.66	0.04	-0.04	0.04	458.42	0.02	0.20	0.20
Set-A_P06	461.19	461.23	0.02	-0.04	0.04	461.17	0.02	0.03	0.03
Set-A_P07	459.75	459.77	0.02	-0.02	0.02	459.74	0.01	0.02	0.02
Set-A_P08	459.00	459.07	0.01	-0.06	0.06	459.00	0.01	0.00	0.00
Set-A_P09	458.45	458.48	0.01	-0.03	0.03	458.33	0.02	0.12	0.12
Set-A_P10	458.51	458.78	0.04	-0.27	0.27	458.74	0.04	-0.23	0.23
Set-A_P11	458.67	458.82	0.01	-0.15	0.15	458.28	0.02	0.38	0.38
Set-A_P12	458.52	458.52	0.01	-0.01	0.01	458.46	0.01	0.06	0.06
Set-A_P13	458.57	458.57	0.02	0.00	0.00	458.60	0.01	-0.03	0.03
Set-A_P14	459.47	459.56	0.02	-0.09	0.09	459.65	0.01	-0.18	0.18
Set-A_P15	458.62	458.66	0.02	-0.04	0.04	458.58	0.02	0.04	0.04
Set-A_P16	457.32	457.29	0.01	0.02	0.02	457.18	0.01	0.14	0.14
Set-A_P17	458.25	458.27	0.01	-0.02	0.02	458.32	0.01	-0.08	0.08
Set-A_P18	458.01	458.03	0.01	-0.01	0.01	457.81	0.01	0.21	0.21
Set-A_P19	457.83	457.84	0.01	-0.01	0.01	457.51	0.02	0.33	0.33
Set-A_P20	458.64	458.64	0.02	0.00	0.00	458.68	0.04	-0.05	0.05
Mean					**0.05**				**0.13**
SD					**0.07**				**0.11**
Set-B_P01	458.26	458.19	0.03	0.07	0.07	458.22	0.02	0.04	0.04
Set-B_P02	458.12	458.13	0.01	-0.01	0.01	458.13	0.02	-0.01	0.01
Set-B_P03	456.53	456.57	0.01	-0.04	0.04	456.32	0.02	0.20	0.20
Set-B_P04	458.01	458.01	0.01	0.00	0.00	457.81	0.01	0.20	0.20
Set-B_P05	459.93	459.95	0.02	-0.03	0.03	460.06	0.02	-0.14	0.14
Set-B_P06	459.92	459.95	0.03	-0.03	0.03	459.86	0.03	0.06	0.06
Set-B_P07	461.09	461.12	0.03	-0.03	0.03	461.10	0.01	-0.01	0.01
Set-B_P08	459.13	459.12	0.02	0.00	0.00	458.81	0.02	0.32	0.32
Set-B_P09	458.66	458.59	0.03	0.07	0.07	458.66	0.02	0.00	0.00
Set-B_P10	458.58	458.61	0.01	-0.04	0.04	458.38	0.03	0.20	0.20
Set-B_P11	459.27	459.28	0.02	-0.01	0.01	459.30	0.02	-0.03	0.03
Set-B_P12	458.75	458.77	0.02	-0.02	0.02	458.80	0.01	-0.05	0.05
Set-B_P13	458.48	458.50	0.01	-0.02	0.02	458.53	0.02	-0.06	0.06
Set-B_P14	457.23	457.24	0.01	-0.02	0.02	457.07	0.01	0.16	0.16
Set-B_P15	458.39	458.40	0.01	-0.01	0.01	458.28	0.02	0.11	0.11
Set-B_P16	458.46	458.47	0.01	-0.01	0.01	458.34	0.03	0.11	0.11
Set-B_P17	458.61	458.71	0.02	-0.10	0.10	458.81	0.03	-0.21	0.21
Set-B_P18	459.38	459.45	0.01	-0.07	0.07	459.39	0.02	-0.01	0.01
Mean					**0.03**				**0.11**
SD					**0.03**				**0.09**

In summary, it should be recalled that TLS is known as an trustworthy and accurate approach for geomorphological studies [4,5,35]. The here generated DEM_{TLS} proves the suitability for capturing the relief of small-scale karstic forms, such as the investigated karst depression. However, low-altitude airborne imaging is increasingly used for geomorphological studies or more generally in physical geography [10,12,36]. The here followed UAV-based approach aims to be simple to perform as well as cost-and time-efficient. In this sense, the post-processing was reduced to a minimum. Vegetation was not removed prior to the DEM generation for example. Considering this, the results of the low-altitude airborne imaging are also satisfying and confirm the promising potential of low-altitude airborne imaging for geomorphological studies.

One aim of the entire project, which was neglected in this contribution, is the detection of temporal changes in the karst depression *Ottensee*. Thus, further research is necessary to investigate whether the accuracy and detailedness of the low-altitude airborne imaging approach is sufficient for detecting changes. Obvious benefits of the UAV-based approach are the very fast data acquisition, the easy handling, and the possibility to capture areas which are not or less accessible with the ground-based laser scanner. In contrast, areas where dense vegetation obscures a nadir perspective can hardly be captured and hitherto available systems are prone to poor weather.

A laser scanner is more robust against poor weather but due to the manual transportation and the measuring time, TLS measurements are quite time consuming. The here used Riegl LMS-Z420i is however quite an old system. Several available newer high-end sensors with the focus on longer scanning ranges, higher measuring rates, or a more lightweight buildup would already diminish some difficulties. Examples are the Riegl VZ-2000 [37] or the Leica Scan Station P40 [38]. A contrasting development are upcoming cost-effective systems like the Velodyne HDL-64E LiDAR sensor [39]. Such systems strongly reduce the cost for TLS measurements and thus increase the availability for a broader audience. Moreover, backpack systems like the AKHKA R2 [40] or hand-held mobile laser scanner such as the ZEB1 [41] might be useful alternatives, as they simplify the data acquisition. So far, such systems are only used in pioneering studies on the detection of trees.

For this study, it can be summarized that the high quality of TLS measurements is worthwhile for capturing small-scale topographic features. Thus, such data sets are still required as trustworthy data for comparative studies with low-altitude airborne imaging. Nevertheless, UAV-based approaches offers a promising time-and cost-effective alternative for the rough acquisition of a terrain. Furthermore, it can be assumed that the entire potential of photogrammetric approaches cannot be evaluated yet since the performance capabilities of such systems are still rapidly increasing. Thus, the combination of laser scanning and photogrammetry-based approaches should be a conceivable option [42–44].

3.2. Images of apparent resistivity

The 2D image of apparent resistivity was created for each ERT profile. Some limitations of the method have to be reconsidered before the interpretation. First, the resistivity values of the different ERT values cannot be compared, since the measured resistivity strongly depends on the moisture content. This soil moisture, in turn, is quite variable over time and space and since the measurements were carried out across a few days, similar conditions cannot be assumed. Second, the depth axis can only be used as rough orientation since the resistivity values are plotted as pseudosections resulting from the inversion model. These pseudosections show the variation of the measured resistivity in relation to the position and the effective depth of penetration. Hence, the 2D images can be used for detecting subsurface structures and changes of material, such as the depth of the bedrock or the existence of different sediment layers. Destructive in-situ measurements, such as borehole drilling, are necessary for accurate statements.

In Figure 5A) the image of apparent resistivity is shown for the 90 m long profile ERT_{01}. Its location is marked in Figure 2. With a thickness of 2 m to 3 m, the reddish superficial layer of the southern part, starting at 0.0 m till ~55.0 m shows the generally highest values of ~60 Ωm to ~100 Ωm. This part of the surface has quite a flat topography, slightly dipping northwards. From the little slope at ~57.6 m northwards the surface is slightly wavy and resistivity variations in the superficial layer between ~30 Ωm to ~60 Ωm can be detected. In this part, the profile crosses the deeper hollow, already stated for the DEMs (Figure 4). Starting again from the southern end of the profile, the yellowish to greenish next layer below the first one, with a thickness of 2 m to 3 m, shows an apparent resistivity of ~20 Ωm to ~50 Ωm. Noteworthy are the three bluish ellipses in the center with lower values of ~0.11 Ωm to ~20 Ωm. Only in the center of the image, another deeper reddish layer with again higher values of ~60 Ωm to ~100 Ωm can be detected.

Based on that image the following geological structure can be supposed (Figure 5B): the deepest lying reddish layer in the center is part of the bedrock. The yellowish to greenish layer is an aquifer made of consolidated soil with clayish lenses, visible as bluish ellipses. The latter are marked by a higher water content and thus a lower resistivity. The reddish superficial layer is made of unconsolidated sediment with a low water content, which might have its origin further uphill, in the south-east of the AOI and which was fluvial deposited. However, one has to keep in mind that the range of the resistivity values is quite small. Thus, the classification used in Figure 5A**)** influences this image interpretation. Further research is necessary to confirm and supplement the here achieved results. As already mentioned, borehole drillings are useful for validating the presumably detected structures. Furthermore, additional ERT profiles can be worthwhile for capturing how these structures change horizontally.

It can be summarized that, images of apparent resistivity derived by geoelectrical measurements are worthwhile for non-destructive investigations of the subsurface and detecting geological structures. The results should be interpreted with care, due to the stated limitations. Further combined analyses with the borehole drillings are planned for the future. The general usability of ERT for detecting karstic structures as shown in other studies [15,16,45] was here confirmed.

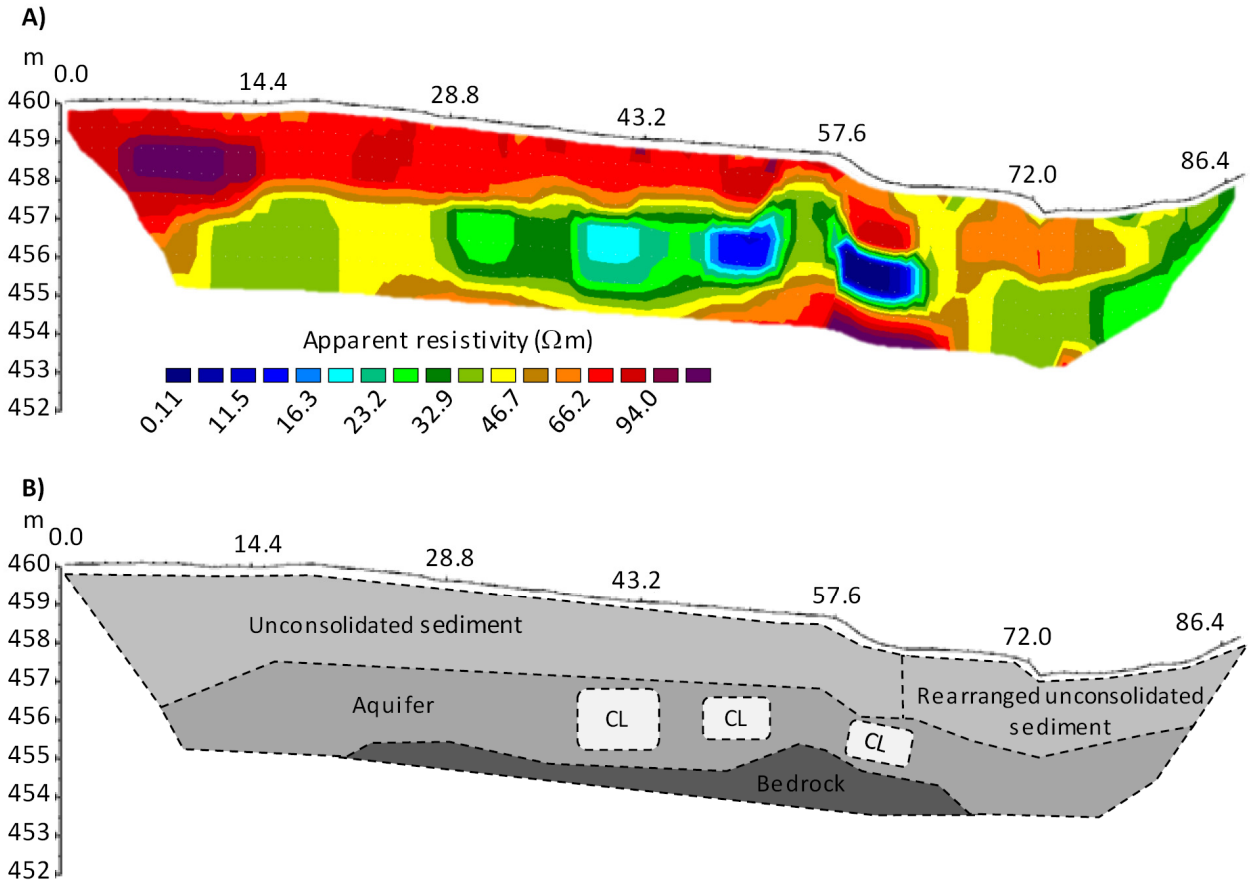

Figure 5. A) Apparent resistivity in the subsurface along the north-south oriented electrical resistivity tomography profile ERT_{01}, location marked in Figure 2. B) Supposed geological structure (CL: clayish lens).

3.3. Block diagrams

The targeted combination of surface and subsurface data was more time-consuming than expected at the beginning. First attempts with the conventionally used tools in Esri ArcScene 10.4.1 did not yield any satisfactory result. The here proposed method (Figure 3) based on the creation of the TIN_{TLS} in the CAD software Geomagic Wrap 2015.1.3 and its visualization in Esri ArcScene 10.4.1 finally yielded good results. An image with oblique perspective to the TIN_{TLS}, which almost represents the bare ground of the karst depression, was used for the pseudo 3D visualizations. The TIN_{TLS} of the entire AOI was previously cut along the ERT profiles for merging it with the 2D images of the subsurface in block diagrams. This is exemplary shown for the profiles ERT_{02} and ERT_{04} in Figure 6. Their locations in the karst depression are shown in Figure 2. In Figure 6 the bluish lines also show the location of the respective other profile for a better orientation. As stated for Figure 5A**)** the range of the resistivity values is quite small, which biases the classification and thus the interpretation. Further investigations on this issue are planned.

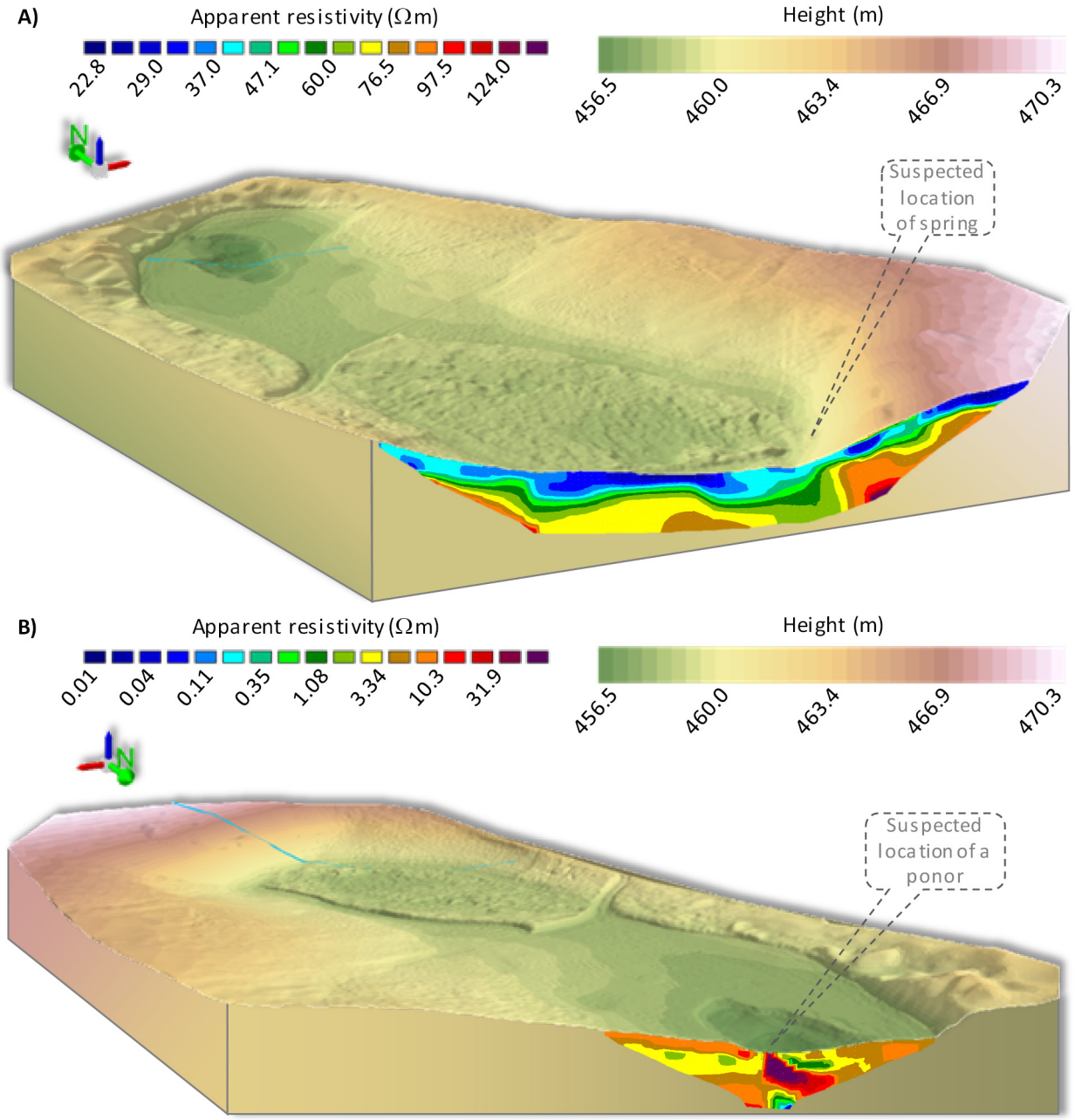

Figure 6. Block diagrams showing the surface captured with terrestrial laser scanning and the apparent resistivity in the subsurface derived by geoelectrical measurements. The surface as triangulated irregular network was cut along two electrical resistivity tomography (ERT) profiles. The bluish lines show the location of the respective other profile. A) View from the south side on the 100 m long ERT_{02} profile. B) View from the north side on the 50 m long ERT_{04} profile.

The 100 m long ERT_{02} profile in the southern part of the depression (Figure 6A) crosses the suspected location of the spring, where subterraneous water reaches the surface. An evidence

therefore might be found in the geoelectrical measurements. The bluish superficial layer indicates low values of apparent resistivity. In the center, this can be attributed to lake sediments, which are saturated with water since this part of the depression is almost constantly filled with water. Trees are located at both ends of the profile, whose roots can enhance the soil water holding capacity and in turn reduce the apparent resistivity. The yellowish to greenish next layer below has a higher apparent resistivity, possibly due to a water-impermeable layer. This layer is closer to the surface at the suspected location of the spring. The deepest reddish layer, indicating the highest apparent resistivity, might be attributed to the bedrock. This assumption can be confirmed with the TIN_{TLS}. Considering that the assumed bedrock is closest to the surface in the eastern part, the TIN_{TLS} shows the highest elevation and steepest slope here as well. Around the spring the slope changes and the surface gets quite flat. The exact boundary of the constantly water-filled area can hardly be determined from the TIN_{TLS}, since the above mentioned mowing of the pasture was not homogeneously possible. Thus, the surface is quite uneven in this part and the height is influenced by the vegetation.

The 50 m long ERT_{04} profile in the northern part of the depression (Figure 6B) crosses the location where one ponor is suspected. A remarkable structure in the image of apparent resistivity is the deep reddish to purplish elongated ellipse in the center of the deep layer that reaches the surface in a small part. This high resistivity might be attributed to very porous and thus water-permeable material, creating good conditions for water to drain off. The overall lowest height value of the TIN_{TLS} can also be found in this part, which confirms this assumption. The yellowish to greenish colors around the ellipse indicate a lower apparent resistivity, which might be interpreted as water-impermeable layer. The small bluish part at the bottom of the image indicates an even lower apparent resistivity, which might be the edge of another layer or just a measurement error. A reliable statement is not possible as the deeper and the more eastern subsurface is unknown. It is worth striving for further ERT measurements in this part of the depression, since another ponor is supposed to be around the eastern end of this profile.

In summary, combing the surface and subsurface data is worthwhile for a better understanding of how the karst depression *Ottensee* was formed and how current changes are occurring. So far, only a few studies on such combined approaches exist. However, Siart et al. [18,19] investigated the combined use of TLS and ERT for achieving a comprehensive presentation of karst landforms and achieved good results. In contrast to the capturing of the surfaces, an issue for common ERT profile measurements is the limitation to 2D acquisitions. Thus, an entire link of surface structures to the underlying subsurface is hardly possible and limited to the analysis of several profiles. Only a few approaches for entirely capturing the subsurface exist so far. One of this is the 3D geoelectric tomography approach, presented by Mauriello et al. [46]. It was successfully applied for detecting archaeological structures by Alaia et al. [47]. A first step for the here investigated karst depression could be increasing the number of ERT profiles, which are ideally arranged raster-like.

4. Conclusion and Outlook

Two main objectives were investigated in this contribution, based on a comprehensive field campaign carried out in May 2016 in the episodically water-filled karst depression *Ottensee*. The first was to investigate the usability of terrestrial laser scanning (TLS) and low-altitude airborne imaging from an unmanned aerial vehicle (UAV) for capturing fine karstic structures. The second objective was to establish a suitable way of combining this surface mapping with subsurface data achieved by geophysical prospecting and examine its benefit. The visualization of the apparent resistivity in the subsurface derived by the electrical resistivity tomography (ERT) measurements is a prerequisite for the latter.

The known trustworthiness and accuracy of TLS was confirmed in this study. Validations against high-accurate reference data sets revealed mean absolute differences of 0.03 m to 0.05 m with a standard deviation of 0.03 m to 0.07 m. Since TLS approaches are however quite time–and cost-intensive, a more efficient approach was pursued for the low-altitude airborne imaging. The latter one has several advantages compared to TLS, regarding the data acquisition and post-processing, such as the use of a low-cost system, quite a short acquisition time, or an extensively automatized post-processing. Disadvantages should however be kept in mind, such as the sensitivity to rain and wind or the lower influenceability of the post-processing, due to this automatized processes. Comparing the results, the discrepancies between the UAV-derived values and the reference data sets are slightly higher, having a mean absolute difference of 0.11 m to 0.13 m with a standard deviation of 0.09 m to 0.11 m.

The spatially calculated difference between the digital elevation models (DEMs) leads to the conclusion, that the weaker performance of the DEM_{UAV} is mainly caused by the vegetation, which was not removed prior to this DEM generation. In summary, the low-altitude airborne imaging approach can be regarded as promising alternative to common remote sensing methods like TLS. However, the detection of suspected temporal changes in the karst depression *Ottensee* was excluded in this contribution. Further field campaigns are necessary to investigate whether the accuracy and detailedness of the low-altitude airborne imaging are sufficient high enough for detecting such changes and whether an accurate merging of the temporal differing data sets is possible.

The visualization of the ERT-derived apparent resistivity as prerequisite for the combined visualization was carried out following conventional methods. Overall, this geophysical prospecting was worthwhile for non-destructively investigate the subsurface and detecting geological structures. However, since only a suspected image of the subsurface can be achieved further research of the subsurface is necessary. The first step will be to analyze the cores taken with borehole drilling in the campaign in May 2016, regarding the material of the subsurface and detecting the specific depths of layer borders. This information might than be used to concretize the ERT-derived results.

The second objective of combining the surface mapping and the suspected image of the subsurface was so far limited to the combination of the latter with the TLS data. Developing the here proposed method was overall more time-consuming than expected at the beginning, but finally satisfying results were achieved. The TLS-derived point cloud was meshed to a triangulated

irregular network (TIN) with a computer-aided design (CAD) software and then visualized with a geographic information system (GIS) software. The CAD software was used since implemented functions allowed an appropriate creating and editing of the TIN_{TLS}. GIS functionalities were however required for the desired visualization, such as coloring the TIN_{TLS} by height and a vertical exaggeration. The final merging of the image with an oblique view on the 3D surface and the 2D image of the apparent resistivity in the subsurface was simple. Establishing a similar approach based on the UAV-derived data is targeted for the future.

The final outlook refers again to one of the main overall aims of this project, namely the detection of suspected temporal changes in the karst depression *Ottensee*. The day after the campaign in May 2016 was marked by heavy rain in south-west Germany. Consequently, the karst depression was filled with water, which lasted several weeks. According to human-based observations, remarkable surface changes occurred. Thus, in the field campaign, already scheduled for June 2017, a remote sensing based detection of changes might be possible.

Acknowledgments

The first initiative for this study came from Dr. Reinhard Zeese, who already carried out plenty of geomorphological studies in the region of Hohenlohe. We would like to thank him for this initiative and for the ongoing knowledgeable support. In this context, we acknowledge the permission for the field campaign by the Agency for Nature Conservation and Landscape Management of Baden-Württemberg. Our thanks also go to Daniel Wunderlich. He is responsible for cultivating and protecting the study area and was always very helpful. For the provision of the geoelectric equipment we thank Prof. O. Bubenzer. The data acquisition was carried out as part of a field experience course with students from the Institute of Geography, University of Cologne. Accordingly, we would like to thank the students for their support, namely A. Berghaus, M. Drahs, S. Esser N. Gerdes, M. Holthausen, M. Kanig, S. Keßler, L. Meine, J. Menne. E. Quix, S. Ranke, A. Symanczyk, F. Weber. In particular, Maximilian Kanig is acknowledged for supervising the geophysical prospecting.

Conflict of interest

All authors declare no conflicts of interest in this paper.

References

1. Zepp H (2014) Geomorphologie. 6th ed. UTB, Stuttgart.
2. Tilly N, Kelterbaum D, Zeese R (2016) Geomorphological mapping with terrestrial laser scanning and uav-based imaging. *Int Arch Photogramm, Remote Sens Spat Inf Sci–ISPRS Arch* 41: 591-597.

3. Large ARG, Heritage GL (2009) Laser Scanning – Evolution of the Discipline. In: Heritage GL, and Large ARG, editors. *Laser Scanning for the Environmental Sciences*, Wiley-Blackwell, West Sussex, UK. 1-20.
4. Buckley SJ, Howell JA, Enge HD, et al (2008) Terrestrial laser scanning in geology: data acquisition, processing and accuracy considerations. *J Geol Soc* 165: 625-638.
5. Tarolli P (2014) High-resolution topography for understanding Earth surface processes: Opportunities and challenges. *Geomorphol* 216: 295-312.
6. Schaefer M, Inkpen R (2010) Towards a protocol for laser scanning of rock surfaces. *Earth Surf Processes Landforms* 35: 417-423.
7. Colomina I, Molina P (2014) Unmanned aerial systems for photogrammetry and remote sensing: A review. *ISPRS J Photogramm Remote Sens* 92: 79-97.
8. Shahbazi M, Sohn G, Théau J, et al. (2015) Development and Evaluation of a UAV-Photogrammetry System for Precise 3D Environmental Modeling. *Sensors* 15: 27493-27524.
9. Turner D, Lucieer A, Watson C (2012) An automated technique for generating georectified mosaics from ultra-high resolution Unmanned Aerial Vehicle (UAV) imagery, based on Structure from Motion (SFM) point clouds. *Remote Sens* 4: 1392-1410.
10. Westoby MJ, Brasington J, Glasser NF, et al. (2012) Structure-from-Motion photogrammetry: A low-cost, effective tool for geoscience applications. *Geomorphol* 179: 300-314.
11. Tong X, Liu X, Chen P, et al. (2015) Integration of UAV-Based Photogrammetry and Terrestrial Laser Scanning for the Three-Dimensional Mapping and Monitoring of Open-Pit Mine Areas. *Remote Sens* 7: 6635-6662.
12. Smith MW, Carrivick JL, Quincey DJ (2015) Structure from motion photogrammetry in physical geography. *Prog Phys Geogr* 1-29.
13. Ouédraogo MM, Degré A, Debouche C, et al. (2014) The evaluation of unmanned aerial system-based photogrammetry and terrestrial laser scanning to generate DEMs of agricultural watersheds. *Geomorphol* 214: 339-355.
14. Butler DK (2005) Near-Surface Geophysics. Society of Exploration Geophysicists. https://doi.org/http://dx.doi.org/10.1190/1.9781560801719.
15. Kidanu ST, Torgashov EV, Varnavina AV, et al. (2016) ERT-based Investigation of a Sinkhole in Greene County, Missouri. *AIMS Geosci* 2: 99-115.
16. Berglund JL, Mickus K, Gouzie D (2014) Determining a relationship between a newly forming sinkhole and a former dry stream using electric resistivity tomography and very low-frequency electromagnetics in an urban karst setting. *Interpret* 2: 17-27.
17. Siart C, Hecht S, Holzhauer I, et al. (2010) Karst depressions as geoarchaeological archives: The palaeoenvironmental reconstruction of Zominthos (Central Crete), based on geophysical prospection, sedimentological investigations and GIS. *Quat Int* 216: 75-92.
18. Siart C, Ghilardi M, Forbriger M, et al. (2012) Terrestrial laser scanning and electrical resistivity tomography as combined tools for the geoarchaeological study of the Kritsa-Latô dolines

(Mirambello, Crete, Greece). *Géomorphol: Relief, Process, Environ* 18: 59-74.
19. Siart C, Forbriger M, Nowaczinski E, et al. (2013) Fusion of multi-resolution surface (terrestrial laser scanning) and subsurface geodata (ERT, SRT) for karst landform investigation and geomorphometric quantification. *Earth Surf Processes Landforms* 38: 1135-1147.
20. Vlahovic T, Munda B (2012) Karst aquifers on small islands-the island of Olib, Croatia. *Environ Monit Assess* 184: 6211-6228.
21. Ahnert F (2009) Einführung in die Geomorphologie. 4th ed. UTB, Stuttgart.
22. Regierungspräsidium Freiburg (2017) Steckbrief Geotope–Ottensee NE von Mulfingen. Available from: http://www4.lgrb.uni-freiburg.de/serverbase/umn/etc/resources/link/gtk/gtk_1812.pdf.
23. Topcon Positioning Systems I (2006) HiPer Pro Operator's Manual. Available from: http://www.top-survey.com/top-survey/downloads/HiPerPro_om.pdf.
24. Riegl LMS GmbH (2010) Datasheet Riegl LMS-Z420i. Available from: http://www.riegl.com/uploads/tx_pxpriegldownloads/10_DataSheet_Z420i_03-05-2010.pdf.
25. DJI (2016) Datasheet Phantom 3. Available from: http://www.dji.com/de/product/phantom-3-adv.
26. DJI (2017) DJI GO app. Available from: http://www.dji.com/goapp.
27. GEO LOG (2017) Multi electrode system GeoTomMK8E1000 RES/IP/SP. Available from: http://geolog2000.de/EN/Geoelektrik/index.htm.
28. Stummer P, Maurer H, Green AG (2004) Experimental design: Electrical resistivity data sets that provide optimum subsurface information. *Geophys* 69: 120-139.
29. Samouëlian A, Cousin I, Tabbagh A, et al. (2005) Electrical resistivity survey in soil science: A review. *Soil Tillage Res* 83: 173-193.
30. Smith RC, Sjogren DB (2006) An evaluation of electrical resistivity imaging (ERI) in quaternary sediments, Southern Alberta, Canada. *Geosph* 2: 287-298.
31. Winters G, Ryvkin I, Rudkov T, et al. (2015) Mapping underground layers in the super arid Gidron Wadi using electrical resistivity tomography (ERT). *J Arid Environ* Elsevier Ltd 121: 79-83.
32. Johnston K, Ver Hoef JM, Krivoruchko K, et al. (2001) Using ArcGIS Geostatistical Analyst. ESRI, USA.
33. Geotomo (2017) RES2DINVx64. Available from: http://www.geotomosoft.com.
34. Loke MH, Barker RD (1996) Rapid least-squares inversion of apparent reistivity pseudosections by a quasi-Newton method. *Geophys Prospect* 44: 131-152.
35. Eltner A, Baumgart P (2015) Accuracy constraints of terrestrial Lidar data for soil erosion measurement: Application to a Mediterranean field plot. *Geomorphol* 245: 243-254.
36. Favalli M, Fornaciai A, Isola I, et al. (2012) Multiview 3D reconstruction in geosciences. *Comput Geosci* 44: 168-176.
37. Riegl LMS GmbH (2015) Datasheet Riegl VZ-2000. Available from: http://www.riegl.com/uploads/tx_pxpriegldownloads/DataSheet_VZ-2000_2015-03-24.pdf.
38. Leica Geoystems (2015) Datasheet Leica ScanStation P40. Available from: http://www.leica-geosystems.com/downloads123/hds/hds/general/brochures-

datasheet/Leica_ScanStation_P30-P40_Plant_DS_en.pdf.
39. Velodyne (2014) Velodyne HDL-64E User's Manual. Available from: http://www.velodynelidar.com/lidar/products/manual/63-HDL64E S2 Manual_Rev D_2011_web.pdf.
40. Liang X, Kukko A, Kaartinen H, et al. (2013) Possibilities of a personal laser scanning system for forest mapping and ecosystem services. *Sens* 14: 1228-1248.
41. Ryding J, Williams E, Smith M, et al. (2015) Assessing Handheld Mobile Laser Scanners for Forest Surveys. *Remote Sens* 7: 1095-1111.
42. Bates KT, Rarity F, Manning PL, et al. (2008) High-resolution LiDAR and photogrammetric survey of the Fumanya dinosaur tracksites (Catalonia): implications for the conservation and interpretation of geological heritage sites. *J Geol Soc* 165: 115-127.
43. Nex F, Rinaudo F (2011) LiDAR or Photogrammetry? Integration is the answer. *Italian J Remote Sens* 43: 107-121.
44. Fabris M, Baldi P, Anzidei M, et al. (2010) High resolution topographic model of Panarea Island by fusion of photogrammetric, lidar and bathymetric digital terrain models. *Photogramm Rec* 25: 382-401.
45. Ahmed S, Carpenter PJ (2003) Geophysical response of filled sinkholes, soil pipes and associated bedrock fractures in thinly mantled karst, east-central Illinois. *Environ Geol* 44: 705-716.
46. Mauriello P, Monna D, Patella D (1998) 3D geoelectric tomography and archaeological applications. *Geophys Prospect* 46: 543-570.
47. Alaia R, Patella D, Mauriello P (2008) Application of geoelectrical 3D probability tomography in a test-site of the archaeological park of Pompei (Naples, Italy). *J Geophys Eng* 5: 67-76.

AIMS Press